

Complex-conductivity monitoring to delineate aquifer pore clogging during nanoparticles injection

Flores Orozco Adrián,¹ Vesna Micić,² Matthias Bucker,³ Jakob Gallistl,¹ Thilo Hofmann² and Frederic Nguyen⁴

¹*Geophysics Research Division, Department of Geodesy and Geoinformation, TU-Wien, Austria. E-mail: flores@tuwien.ac.at*

²*Environmental Geosciences, Centre for Microbiology and Environmental Systems Science, University of Vienna, Austria*

³*Institute of Geophysics and Extraterrestrial Physics, TU Braunschweig, Germany*

⁴*Urban and Environmental Engineering, University of Liege, Belgium*

Accepted 2019 May 31. Received 2019 May 5; in original form 2019 January 15

SUMMARY

Laboratory and field studies have demonstrated the applicability of nanoparticles (NP) for accelerated contaminant degradation. Beside other limitations (e.g. costs, delivery, longevity, non-target specific reactions), concerns of regulators arose regarding toxicity of injected NP and particles delivered off-target (i.e. renegade particles). Renegade particles also significantly reduce the efficiency of the remediation. The delivery of particles off-target is caused, mainly, by unintended fracking, where the fractures act then as preferential flow paths changing the trajectory of the particles. Hence, the real-time monitoring of particle injection is of major importance to verify correct particle delivery and thus help to optimize the remediation strategy. However, to date NP monitoring techniques rely on the analysis of soil and water samples, which cannot provide information about clogging or the formation of fractures away of the sampling points. To overcome these limitations, in this study we investigate the applicability of complex-conductivity imaging (CCI), a geophysical electrical method, to characterize possible pore clogging and fracking during NP injections. We hypothesize that both processes are related to different electrical footprints, considering the loss of porosity during clogging and the accumulation of NP in areas away of the target after fracking. Here, we present CCI results for data collected before and during the injection of Nano-Goethite particles (NGP) applied to enhance biodegradation of a BTEX (benzene, toluene, ethylbenzene and xylene) contaminant plume. Imaging results for background data revealed consistency with the known lithology, while overall high electrical conductivity values and a negligible induced-polarization magnitude correspond with the expected response of a mature hydrocarbon plume. Monitoring images revealed a general increase (~15 per cent) in the electrical conductivity due to the injected NGP suspension in agreement with geochemical data. Furthermore, abrupt changes in this trend, shortly before daylighting events, show the sensitivity of the method to pore clogging. Such interpretation is in line with the larger variations in CCI resolved in the unsaturated zone, clearly indicating the accumulation of renegade NGP close to the surface due to fracking. Our results demonstrate the applicability of the CCI method for the assessment of pore clogging accompanying particles injection.

Key words: Hydrogeophysics; Electrical resistivity tomography (ERT); Permeability and porosity; High-pressure behaviour.

1 INTRODUCTION

An extensive number of laboratory studies have demonstrated that nanoparticles (NP) could speed up the degradation of groundwater contaminants, taking into account their large specific surface area and high surface reactivity (for a review see Grieger *et al.*

2010; Trujillo-Reyes *et al.* 2014; Adeleye *et al.* 2016 and references therein). Moreover, NP injection offers a promising cost-effective approach for the *in-situ* remediation of contaminated areas inaccessible for other techniques such as deep contaminant plumes, areas beneath infrastructure, as well as for multisource contaminated areas in low hydraulic permeable media (e.g. Karn *et al.* 2009; Tosco

et al. 2014 and references therein). Given their relatively low costs, zero-valent iron (ZVI) and iron-oxide NP have become popular due to their ability to promote the degradation of a variety of pollutants (e.g. Grieger *et al.* 2010; Tosco *et al.* 2014; Velimirovic *et al.* 2014; Chen *et al.* 2015; Schmid *et al.* 2015; Bhattacharjee & Ghoshal 2018). Iron-oxide particles are of special interest due to their non-toxicity, adsorption capacity and ability to stimulate bioremediation (Hua *et al.* 2012; Xu *et al.* 2012; Braunschweig *et al.* 2013; Lei *et al.* 2018). Especially, goethite (α -FeOOH) has demonstrated a high sorption capacity for metal cations (e.g. Hua *et al.* 2012), as well as the potential to enhance contaminant degradation by iron-reducing bacteria (Bosch *et al.* 2010). Specifically, ferric iron can act as an electron acceptor for microbial respiration (Fe³⁺-reduction coupled with the oxidation of contaminants) and can overcome limitations in electron-acceptor availability.

Results observed in laboratory have encouraged field-scale NP injections, with pilot and full-scale experiments reported to date in 92 sites worldwide (e.g. Mueller *et al.* 2012; Patil *et al.* 2016; Bardos *et al.* 2018 and including interactive map). Yet, there are still concerns regarding the effective delivery to the targeted areas and potential toxicity of the particles (e.g. Grieger *et al.* 2010; Bianco *et al.* 2017). Subsurface heterogeneities play an important role in the actual trajectory of the injected particles, for instance unintended injections into preferential flow paths might lead to particles traveling off target. Nathanail *et al.* (2016) adopted the term 'renegade particles' to describe those NP that deviate from the intended trajectory, either not reaching the targeted pollutant or passing through it. A particular case refers to the so-called daylighting, the incident in which renegade particles emerge to the surface along preferential flow paths, for instance through fractures developed by non-intended fracking. Fracking results from pressure building up during the NP injections due to continuous injections performed at high pressure (Hosseini & Tosco 2015; Luna *et al.* 2015), as well as from clogging of the pore space following aggregation and sedimentation of the injected particles (e.g. Tosco & Sethi 2010) enhanced by slow injections (e.g. Luna *et al.* 2015).

Hence, the real-time assessment of pore clogging during NP injection offers the opportunity to relocate the injection and may be the best approach to minimize unintended fracking and, thus, improve the efficiency of NP delivery into the target zone. However, to-date, the monitoring of NP injections still relies on direct methods based on the analysis of soil and groundwater samples (Tosco *et al.* 2014). Although such methods provide information about chemical parameters of interest, they are not suited for real-time monitoring and cannot identify pore clogging.

Geophysical methods can provide essential information about subsurface properties in quasi real-time and with high spatial resolution, offering a unique possibility to identify pore clogging during NP injections. In particular, the complex-conductivity imaging (CCI) method appears to be a suitable technique, considering that laboratory investigations have demonstrated the ability of the method to gain information about pore-space properties (e.g. grain size, pore length) controlling water flow (e.g. Slater 2007; Revil & Florsch 2010; Kemna *et al.* 2012; Okay *et al.* 2013; Binley *et al.* 2016; Gallistl *et al.* 2018; Mainault *et al.* 2018). Based on the electrical properties of contaminants, the CCI has also shown to be a well-suited method for characterization of contaminated sites (e.g. Deceuster & Kaufman 2012; Flores Orozco *et al.* 2012a; Johansson *et al.* 2015; Deng *et al.* 2018; Ntarlagiannis *et al.* 2018). Moreover, it has been observed that microbial activity also modifies the CCI response, either by the electrical properties of the microbial cells

themselves (e.g. Revil *et al.* 2012) or by induced chemical transformations (e.g. Atekwana and Slater 2009; Abdel Aal *et al.* 2014 and references therein). Built on such observations, the method has also been applied at the field-scale for the monitoring of bio-geochemical processes accompanying a variety of remediation techniques (e.g. Slater & Binley 2006; Williams *et al.* 2009; Flores Orozco *et al.* 2011; Chen *et al.* 2012; Saneiyani *et al.* 2019).

Regarding NP investigations, column studies have demonstrated variations in the electrical response due to different nanoparticles (e.g. Joyce *et al.* 2012; Abdel Aal *et al.* 2017; Mellage *et al.* 2018). However, only the study of Flores Orozco *et al.* (2015) has reported the application of the CCI method at the field scale. The authors revealed changes in the electrical images associated with accumulation of bare and coated microscale ZVI particles.

In this study, we extend previous investigations to evaluate the capabilities of the CCI method to monitor the fate and transport of a suspension of nano-goethite particles (NGP) injected in a BTEX-contaminated site. CCI measurements were conducted at the field scale with high temporal resolution aiming at identifying potential pore clogging due to particle sedimentation. The possible pore clogging indicated by the electrical images is supported by extensive geochemical data. Information on pore clogging and the reduction of hydraulic conductivity is critical towards the development of strategies for the effective delivery of NP and the improved remediation of contaminant plumes. To our best knowledge, this is the first field-scale study presenting the CCI monitoring results along nanoparticles injections.

2 MATERIAL AND METHODS

2.1 Pilot site: Spolchemie II in the Czech Republic

Our study presents imaging results for data collected during the injection of NGP at the Spolchemie II site within the scope of the NanoRem project. The Spolchemie II site is located in an industrial area near Ústí nad Labem (Czech Republic) characterized by an unconfined aquifer underlain by a clay layer of low hydraulic permeability at a depth of ~ 10 m; while an anthropogenic layer (with a thickness of ~ 1 m) covers the surface. The aquifer, located below this anthropogenic layer, is composed of quaternary sediments, mainly sand and gravel, with a hydraulic conductivity of $\sim 5.9 \times 10^{-5} \text{ m s}^{-1}$, and the main groundwater flow goes in south-eastern direction (NanoRem Bulletin 8). The groundwater table was found at 5 m below ground level (bgl) during our experiments.

The production of synthetic resin as well as the storage of various raw materials at the site has led to extensive groundwater contamination by BTEX compounds, with toluene representing the main contaminant, followed by xylene and ethylbenzene, and a negligible amount of benzene. The experimental area for the NP injection covers an area of approximately $10 \times 10 \text{ m}^2$, where seven existing wells permit the collection of groundwater samples for geochemical analysis (Fig. 1). At the time of our experiments, BTEX concentration at the water table exceeded 50 mg l^{-1} (as presented in Fig. 1), with lower concentrations for samples collected at larger depths, as expected considering that BTEX compounds are light non-aqueous phase liquids (LNAPL).

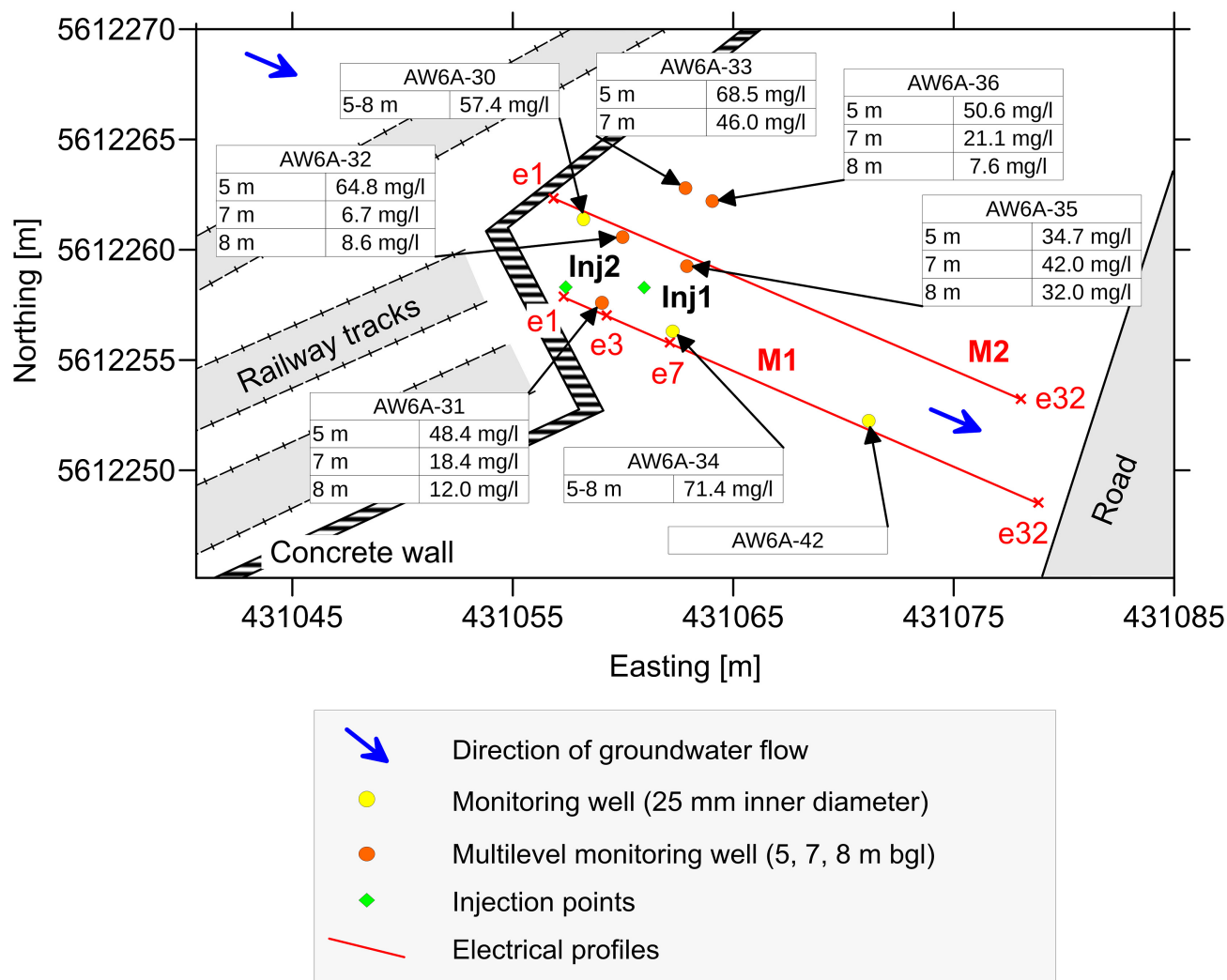


Figure 1. Schematic plan view of the Spolchemie II, CZ site, indicating the position of the monitoring wells and the injection points, BTEX concentrations (in mg l^{-1}) in the monitoring wells, as well as the layout of the electrical profiles M1 and M2 (red lines). The shaded areas indicate the position of infrastructure such as buildings, roads, etc.

2.2 Nano-Goethite particles, particle injections and geochemical monitoring

NGP coated with humic acids to reduce particle aggregation and enhance their mobility (Tirafferri *et al.* 2017), were provided in a stock suspension by the University of Duisburg-Essen and are described elsewhere (Meckenstock & Bosch 2014). The injection suspension was prepared on site by diluting the stock suspension with the filtrated water from the nearby Elbe River and adding a potassium-bromide (KBr) tracer and stored in two tanks.

The injection suspension was intended to contain a particle concentration of 5 g l^{-1} , aiming at delivering a total of 300 kg of NGP. Injections were planned between 5 and 8 m bgl (from top to bottom) in half-metre intervals at low pressure (between 1 and 12 bars) using a direct-push probe. Although injections were planned at five locations, in this study we are only presenting results observed for injections performed at two locations (Inj1 and Inj2 as depicted in Fig. 1) while groundwater sampling was possible. Clogging of the observations wells (as described in the following sections) hindered sampling required for geochemical analysis and therefore will not be presented here.

Prior to the NP injection, geochemical measurements were performed in all observation wells using the membrane-interface well logging probe (MIP) Ecoprobe-5 (from RS Dynamics). The Ecoprobe-5 is equipped with a photo-ionization detector (PID) and an InfraRed (IR) sensor permitting the *in-situ* screening for total petroleum hydrocarbons (TPH) and volatile organic compounds (VOC). For the monitoring of geochemical parameters upon the NGP injections, seven observation wells were available. Five of those were equipped with micro pumps at 5, 7 and 8 m bgl (multi-level monitoring wells). Two additional observation wells, screened between 4 m and 8 m bgl, were situated up- and down-gradient from the injection points aiming at the detection of renegade NP. Along the NGP injection, *in-situ* groundwater parameters, such as temperature, electrical conductivity (i.e. fluid conductivity, σ_f), pH and redox potential, were determined with calibrated probes. It was not possible to employ an on-site turbidity probe, as the diameter of the turbidity probe exceeded that of the groundwater monitoring well. Therefore, turbidity was determined in non-filtered groundwater samples upon return to the laboratory using a turbidimeter 2100 N IS (Hach Lange, Germany) calibrated with formazine standards. Total iron (Fe_{tot}) content in groundwater samples, determined by

ICP-OES Optima 5300DV (PerkinElmer, USA) after acid digestion (with 30 per cent HCl and 5 M HNO₃), was used as a proxy of NGP concentration.

2.3 Indirect monitoring method: complex-conductivity imaging

Complex-conductivity measurements, also referred to as induced polarization (IP), are based on four-electrode arrays and can be performed in the time- or frequency-domain (Ward 1990). When performed in the frequency-domain (as in this study), two electrodes are used to inject a sinusoidal current to the ground, and the second pair of electrodes is used to record the associated phase-shifted voltage. The deployment of tens of electrodes, for the collection of hundreds of measurements, permits to solve for spatially quasi-continuous models (i.e. images) of the subsurface complex conductivity (Binley & Kemna 2005; Kemna *et al.* 2012). The real (σ') and imaginary (σ'') components of the complex conductivity (σ^*) represent the low-frequency (<1 kHz) electrical conductivity (i.e. energy loss) and capacitive (i.e. energy storage) properties of the subsurface, which can also be expressed in terms of magnitude ($|\sigma|$) and phase (ϕ):

$$\frac{1}{\rho^*} = \sigma^* = \sigma' + i \sigma'' = |\sigma| e^{i\phi}, \quad (1)$$

where $i = \sqrt{-1}$ represents the imaginary unit. In most subsurface investigations, the values of ϕ are sufficiently small (<100 mrad), such that $\sigma' \approx |\sigma|$, which is typically referred to as the electrical conductivity (σ) or its inverse the electrical resistivity ($\rho = 1/\sigma$). Equally, for sufficiently small values, the phase of the complex conductivity can be approximated by the ratio of the imaginary to the real component ($\phi \approx \frac{\sigma''}{\sigma'}$), which has been also suggested as a valid proxy to quantify the IP effect.

In most subsurface materials, electrical conduction is carried by the electrolyte (i.e. ionic conduction) and through the electrical double layer (EDL) covering the pore surface (e.g. Waxman and Smits 1968; Leroy *et al.* 2008, and references therein). Ionic conduction is controlled by porosity, saturation and fluid conductivity (σ_f) (e.g. Slater 2007 and references therein); surface conduction along the EDL mainly depends on surface charge and surface area (Schwarz 1962; Schurr 1964; Leroy *et al.* 2008). For clay and other materials characterized by high surface charge and surface area, surface conduction is the dominating conduction mechanism under most conditions (i.e. for low and intermediate ionic strengths of the pore water) and commonly related to high σ values (e.g. Marshall & Madden 1959; Revil & Florsch 2010).

The IP effect in such (metal-free) media results from the migration and accumulation of charge carriers within the different parts of the EDL and has been described by means of two principle mechanisms (e.g. Kemna *et al.* 2012 and references therein): (i) the polarization of the Stern layer (e.g. Leroy *et al.* 2008; Revil & Florsch 2010; Revil *et al.* 2017) or the diffuse layer (e.g. Fixman 1980; Shilov *et al.* 2001) around isolated mineral grains; and (ii) the polarization of overlapping diffuse layers in pore throats better known as membrane polarization (Marshall & Madden 1959; Ward 1990; Bückler & Hördt 2013; Hördt *et al.* 2017). If highly conductive inclusions are present as a discontinuous phase (e.g. metallic nanoparticles or disseminated minerals), the conductor–electrolyte interfaces polarize giving rise to a strong polarization response. This so-called electrode polarization has been described for perfectly conducting inclusions, such as metallic conductors

(e.g. Wong 1979; Bückler *et al.* 2018) and more recently for semi-conducting inclusions, such as most natural metal ores (e.g. Revil *et al.* 2015; Misra *et al.* 2016).

2.4 Complex-conductivity imaging monitoring set-up

CCI monitoring data sets were collected in the frequency domain (at 1 Hz) using the eight-channel DAS-1 (from Multi-Phase technologies) along two profiles (M1 and M2, as depicted in Fig. 1). Each profile comprised 32 electrodes with a separation of 0.75 m between electrodes, aiming at a depth of investigation of 8 m. The presence of concrete walls and roads impeded to extend the length of the profiles for a larger investigation depth. A multiple-gradient configuration (Dahlin & Zhou 2006) was used for both profiles with eight potential dipoles (with lengths of $a = 0.75, 1.5, 2.25$ and 3 m) nested within the current dipole yielding 380 quadrupoles per profile. We opted for this electrode configuration considering that it provides measurements with a larger signal-to-noise ratio (S/N) than other configurations (Dahlin & Zhou 2006; Flores Orozco *et al.* 2018a). Moreover, initial measurements proved sensitive within the required depth of investigation (between 5 and 8 m bgs) and showed negligible distortions due to anthropogenic noise. Monitoring data sets were collected independently along each transect, i.e., no 3-D acquisition schemes to reduce the acquisition time. We aimed at collecting an entire data set in less than 7 min to enhance the temporal resolution of the CCI monitoring. The only gaps in the CCI monitoring corresponds to the overnight break, where the instrument needed to be retrieved from the field.

For the inversion of the observed CCI data, we used CRTomo, a finite-element smoothness-constraint algorithm (by Kemna 2000), which solves for the subsurface distribution of σ^* . This algorithm was selected, as it permits to fit the data within the inversion to a confidence interval, which is defined by an error model (e.g. Kemna 2000; Flores Orozco *et al.* 2012b). Such approach minimizes the risk of overfitting the data during the inversion and the associated creation of artefacts (e.g. Kemna 2000; Slater & Binley 2006; Flores Orozco *et al.* 2012b; Lesparre *et al.* 2017). Blanked areas in the imaging results correspond to regions associated with cumulated sensitivity values two orders of magnitude smaller than the highest cumulated sensitivity (i.e. the sum of absolute, data-error weighted, sensitivities of all considered measurements; see e.g. Weigand *et al.* 2017).

The error model aims at describing the magnitude of random error present in the data; yet it cannot be used to describe a systematic error. Hence, as a first step in the data processing, we removed physically implausible measurements, namely those associated with a negative current amplitude, geometrical factor or apparent resistivity. Then we performed a histogram analysis as proposed by Flores Orozco *et al.* (2018b) to assess the spatial consistency within the data set. Such approach suggests that the occurrence of empty bins in the histogram can be used to define maximum and minimum threshold values in the measured resistances and apparent phase-shift. Yet, no measurement was removed after those analyses demonstrating the good quality of the data. To better illustrate this, we present in the complementary material exemplary pseudo-sections for data collected at different time-lapses.

The analysis of normal and reciprocal readings has been widely accepted for the quantification of random error (e.g. Slater *et al.* 2000; Flores Orozco *et al.* 2012b). However, the fast process under investigation in this study and the collection of gradient configurations limited the possibility to collect reciprocal readings. Hence,

error parameters were estimated based on the analysis of the data quality computed by the instrument (standard deviation from three repetitions) and for the linear error model (e.g. Slater *et al.* 2000)

$$\varepsilon(R) = a + bR, \quad (2)$$

where, a and b refer to an absolute ($a = 1 \text{ m}\Omega$ in our study) and relative ($b = 5$ per cent in our study) error parameters (Slater *et al.* 2000). In case of phase measurements, we used a constant error equal to 1 mrad (e.g. Slater & Binley 2006). All inversion results presented here converged to a root-mean-square (RMS) equal to 1, where the RMS refers to the error-weighted misfit between the data and the modelled forward response (for a comprehensive description of the inverse modelling, we refer to Kemna 2000). CCI monitoring data sets were processed and independently.

3 RESULTS AND DISCUSSIONS

3.1 Background electrical imaging results delineate lithology and contamination levels

Background measurements were collected approximately 24 hr before the first NGP injection. Fig. 2 presents imaging results for background data expressed in terms of the electrical conductivity ($|\sigma|$) and the IP effect (ϕ) along M1, where lithological information is available (core drilling of the observation well AW6-42). Imaging results for background data collected along M2 are consistent to those presented in Fig. 2 (data not shown). The top panel of Fig. 2 shows that spatial variations in the electrical conductivity ($|\sigma|$) are in agreement with lithological changes. The lowest $|\sigma|$ values ($<50 \text{ mS m}^{-1}$) correspond with unsaturated loess and sandy gravels, with a slight increase in $|\sigma|$ associated to the occurrence of finer grains (sandy gravel) at depths between 4 and 5.5 m bgl in the unsaturated zone. The highest $|\sigma|$ values ($>80 \text{ mS m}^{-1}$) below 5.5 m bgl correspond with the saturated sandy clay. The ϕ image presented in the bottom panel of Fig. 2 shows no clear correlation with the lithological units. While the lower part of the image ($<2\text{--}4$ m bgl) is dominated by low values (<5 mrad), the shallow part of the image reveals locally high IP responses, yet these anomalies are most likely due to anthropogenic structures (e.g. pipes, backfill material).

The presence of two shallow cast-iron pipes (located at a depth between 1 and 2 m) is reported at the site, approximately at 7 and 15 m (along direction of profile M1). The pipes have a diameter of 12 cm (smaller than a fifth of the electrode separation), and are coated and wrapped with rubberized products to prevent contact with soil and groundwater and hinder corrosion. Such coating explains the lack of an IP response, as expected due to electrode polarization typical of blank metallic structures. Nonetheless, small phase anomalies ($\phi \sim 3$ mrad) can be distinguished in the shallow areas (between the surface and 2 m depth), which may be related to the heterogeneities in the anthropogenic (gravel) layer around the pipes and likely also distort the magnitude image in the shallow areas (1–2 m depth). Hence, monitoring imaging results presented in this study are only related to model parameters below 2 m depth, at which the distortion caused by the anthropogenic structures might be negligible (e.g. Flores Orozco *et al.* 2012a; Flores Orozco *et al.* 2019).

BTEX compounds are non-polar and, thus, tend to form droplets caged between the water molecules; these are also referred to as non-wetting hydrocarbons considering that they are not in direct contact with the grain surfaces (e.g. Schmutz *et al.* 2010). Early

laboratory investigations on non-wetting hydrocarbons reported an increase in the IP effect for increasing hydrocarbon concentration (e.g. Olhoeft 1985). Based on laboratory observations, an empirical model was proposed by Schmutz *et al.* (2010), which predicts a monotonous increase in the polarization response with increasing saturation of non-polar hydrocarbons (e.g. toluene). Such model is based on the polarization of the Stern layer and incorporates variations of the polarization response due to the presence of an electrically insulating and non-polarizable contaminant. A recent study demonstrated its applicability for laboratory measurements conducted on clayey soils (Deng *et al.* 2018).

At the same time, recent studies have revealed the opposite response, that is, a decrease of the polarization response with increasing saturation of hydrocarbon contaminants, at frequencies below 100 Hz (e.g. Schwartz *et al.* 2012; Ustra *et al.* 2012; Shefer *et al.* 2013). This behaviour may be explained by an increase of the wettability of the non-polar hydrocarbons, as proposed by Revil *et al.* (2011). These authors suggest that absorption of polar compounds to the grain surface will result in an increase of the bulk conductivity and a decrease of the polarization response. Microbial activity is also known to increase the wettability of hydrocarbons, due to the release of metabolic products that change the electrical properties of the hydrocarbons (e.g. Cassidy *et al.* 2001).

Investigations at the field scale (Flores Orozco *et al.* 2012a) have permitted to differentiate two behaviours: (i) a linear increase of the IP response ϕ for BTEX concentrations below the saturation concentration of the hydrocarbon; and (ii) a negligible IP response ($\phi < 5$ mrad) for hydrocarbon concentrations above the saturation concentration—at which the contaminant is present in free-phase. The change in the IP response around the saturation concentration has also been studied by Bucker *et al.* (2017) based on an analytical membrane-polarization model. These authors argue that low BTEX concentrations are related to the presence of small isolated hydrocarbon droplets within the large macro pores and a large membrane-polarization effect (i.e. an increase in ϕ) is caused by the small ion-selective pore throats, which are essentially contaminant free, if the hydrocarbon is non-wetting. However, if hydrocarbon concentration increases, the contaminant phase becomes continuous and fills both macro pores and pore throats, hindering the formation of ion-selective throats and, thus, reducing the IP effect (Bucker *et al.* 2017). Based on this model, the negligible IP response observed in Fig. 2 seems to be a consequence of toluene concentrations, which in fact exceed saturation concentration at the study site (saturation concentration of toluene is around 520 mg l^{-1}).

3.2 Mature hydrocarbon plumes show an increased electrical conductivity

Chemical transformations of hydrocarbon contaminant plumes may change the electrical footprint sensed in the subsurface, as observed in laboratory investigations (e.g. Heenan *et al.* 2014; Ntarlagianis *et al.* 2018 and references therein). Besides this, hydrocarbon plumes represent a source of organic carbon, which may stimulate microbial activity (Huling *et al.* 2002). Microbial activity enhances the transformation of contaminants (e.g. Schirmer *et al.* 2006), as well as the release of metabolic products, such as carbonic acids, commonly resulting in an increase of fluid conductivity and, thus, of the bulk electrical conductivity $|\sigma|$ (e.g. Atekwana & Atekwana 2010; Cassiani *et al.* 2014; Heenan *et al.* 2014; Caterina *et al.* 2017 and references therein). Moreover, carbonic acids have also been related to grain weathering and the development

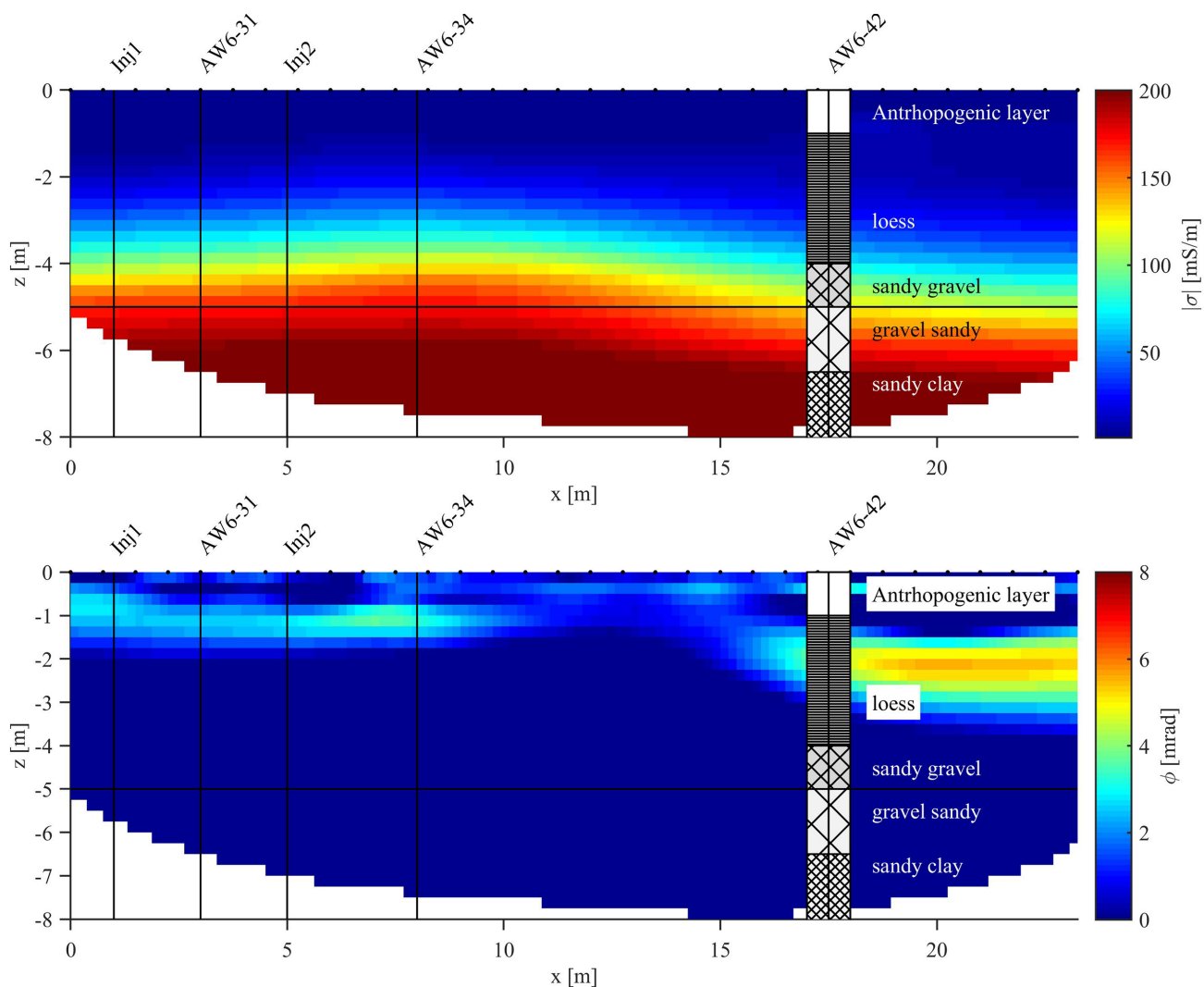


Figure 2. Electrical imaging results for data collected one day prior to the NGP injection expressed in terms of the magnitude ($|\sigma|$) and phase (ϕ) of the complex electrical conductivity. The positions of the monitoring wells (AW6-31, AW6-34 and AW6-42) and the injection points are indicated (solid vertical lines), as well as the depth to the groundwater table during the experiments (solid horizontal line). The overimposed lithological log of well AW6-42 aids the interpretation of the electrical units.

of secondary porosity and biofilms, further increasing the electrical conductivity of mature hydrocarbon plumes (Abdel Aal *et al.* 2004; 2006). Hence, chemical transformations related to a mature contaminant plume explain the high $|\sigma|$ values observed in Fig. 2, which might seem to be in contradiction to the low conductivity of fresh hydrocarbon spills (Cassiani *et al.* 2009). Furthermore, an increase in σ_f also has an effect on the IP response, as it reduces the contribution of the EDL to the overall conduction and, thus, further decreases the ϕ due to membrane polarization (Hördt *et al.* 2016).

TPH and VOC well-logs revealed high values around the water table (~ 5 m bgl), which was in agreement with the analysis of groundwater samples (Fig. 1) and the highest $|\sigma|$ values observed in Fig. 2. Moreover, MIP measurements of methane (CH_4) and carbon dioxide (CO_2) also revealed high concentrations in both the vadose and the saturated zone (Fig. 3), likely due to the stimulated microbial activity at the site, supporting the interpretation of the electrical images presented above.

3.3 Daylighting and other problems observed during the injection of the nano-goethite particles

NGP injection began at well Inj1 using the suspension from the first storage container, which at the site revealed a larger than intended particle concentration (ca. 20 g l^{-1} measured in the storage tank). The particle injection at the first, second and third injection depth (5, 5.5 and 6 m bgl in Inj1) were performed at a low pressure (5–6 bar, for a duration of ~ 75 min at each depth) aiming at preventing fracturing. Nevertheless, even if the injections were performed at low pressures, during the third injection (at 6 m bgl) in Inj1, solution escaped to the surface (daylighting) through wells AW6-30, AW6-31 and AW6-32 (a picture from the field conditions during daylighting is presented in Fig. 4). Furthermore, daylighting was also occurring at observation well AW6-30, which is located up-gradient from Inj1, clearly indicating the transport of particles away from the target areas and opposed to the main direction of groundwater flow, sustaining the interpretation of ongoing pore clogging close to the injection point.

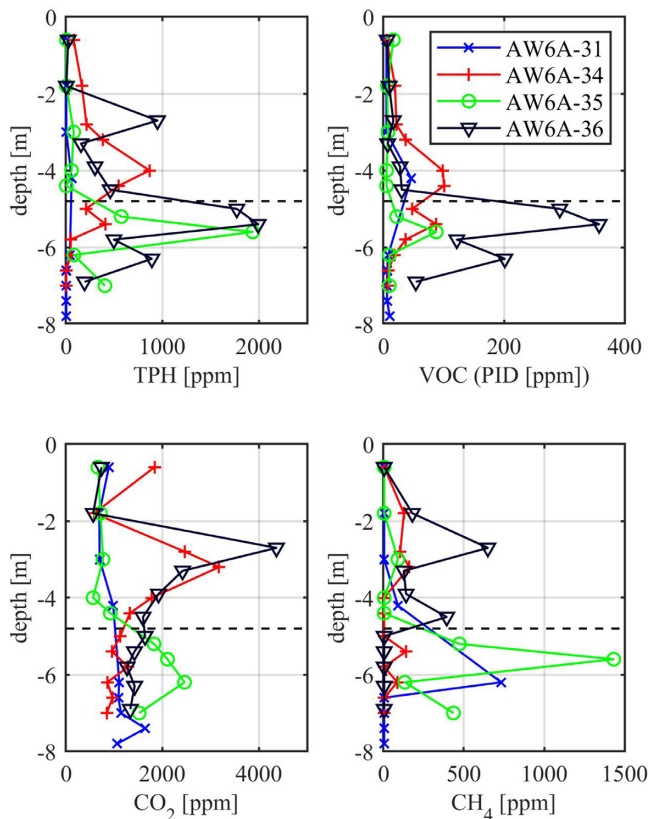


Figure 3. Geochemical data in selected monitoring wells measured *in situ* prior to the injection of the NGP. TPH: total petroleum hydrocarbons, VOC: volatile organic compounds. Data provided by AQUATEST a.s. (CZ).

NGP injections became less regular after the first daylighting; namely, injection in Inj1 at 6 m depth was suspended after a few minutes due to solution flowing to the surface. Injections at the next depth (6.5 m) were performed at higher pressure (>10 bar) to force the delivery of NGP in the subsurface, but after a few minutes, suspension was again flowing to the surface hindering further injection at that depth. At this point, the solution flowing out near the observations wells AW6-30, 31 and 32 was visibly containing iron (see picture in Fig. 4). To allow the delivery of the slurry, injections at 7 and 7.5 m depth were performed at even higher pressure (>12 bar), reducing the injection time to ~40 min for each step.

Injections at the second injection point (Inj2) started ~50 min after the last amendment in Inj1, at depths of 5, 5.5 and 6 m (at 12 bar and a delivery time of ~40 min). Yet, suspension flowing to the surface still occurred in several observation wells during the injection periods. Furthermore, geochemical sampling was hindered due to clogging of the tubing in observation wells affected by daylighting.

After an overnight break, which impeded the collection of CCI and geochemical data, NGP injections were restarted using suspension from the second container (initial particle concentration of ca. 10 g l^{-1}). During the second day, NGP injections were performed at 6.5, 7 and 7.5 m in Inj2 (also at 12 bar). Yet, daylighting was observed also for these injections and geochemical sampling was compromised again. Hence, in the following sections, we do not consider further injections points and only present results for data collected during the delivery of the NGP suspension from the first container in Inj1 (all injection depths) and Inj2 (only down to 6.5 m bgl).

3.4 Electrical monitoring images evidence fracking following particles injection

CCI measurements were collected every 7 min along the monitoring transect (i.e. profiles M1 and M2), with a long break overnight due to safety regulations within the facilities. CCI monitoring data sets were processed and inverted independently before the calculation of percentage changes between the baseline and the monitoring imaging results, as presented in Fig. 4.

As discussed above, anthropogenic structures close to the surface resulted in the creation of artefacts in the electrical images within the first 1 m depth. Under similar conditions, earlier studies have demonstrated the capability of the CCI method to characterize subsurface processes accurately at depths below the anthropogenic structures (e.g. Flores Orozco *et al.* 2012a, 2015; Caterina *et al.* 2017; Lesparre *et al.* 2017). Accordingly, here, we present only the temporal changes below the cover layer (between 1 and 8 m bgl), which reveal consistent results during the entire experiment, as observed in exemplary images presented in Fig. 4. Monitoring data sets in profile M2 were mainly collected along the injection of the solution of the second NGP storage tank and, as mentioned above, are not further discussed.

The imaging results in Fig. 4 show a modest increase (~10 per cent) in $|\sigma|$ in the saturated zone after concluding the first NGP injection (at 5 m depth). Images for data collected at later times (and injections) reveal a further increase in $|\sigma|$, with the last images, showing an increase of up to ~20 per cent in the electrical conductivity of the saturated zone, when compared to the baseline image. These recorded changes in the electrical conductivity correspond to subsurface amendment of NGP suspension, characterized by a fluid conductivity (σ_f) ~27 per cent higher than the groundwater (Table 1).

The increase in $|\sigma|$ (between 10 and 20 per cent over baseline measurements) in Fig. 4 close to the injection wells is clearly related to the addition of the NGP suspension. Nevertheless, changes in the electrical properties are not only confined to the depth of the NGP injection (between 5 and 8 m bgl), but are also observed in the unsaturated zone, in particular, between 2 and 4 m bgl. A straightforward explanation for such variations is that fractures developed during the NGP delivery extended from the injection point to the unsaturated zone, which led to the accumulation of the injected solution containing free humic acids, and likely NGP, close to the surface. The accumulation of particles away from its initial target has been previously reported for field-scale particles injection (e.g. Flores Orozco *et al.* 2015; Luna *et al.* 2015).

The impossibility to collect water samples in the unsaturated zone hinders the quantitative interpretation of the CCI anomalies. Nevertheless, our interpretation of the shallow electrically conductive anomaly is supported by the occurrence of daylighting in monitoring wells AW6-31 and AW6-32 during the third injection step (at 6 m bgl). Following this argumentation, the shallow conductive anomaly observed in Fig. 4 (after a few minutes after starting the very first injection) indicates that the fracking started much earlier than the daylighting (~160 min after starting the first injection), likely already during the first injection in Inj1 (at 5 m bgl). The position of the main conductive anomaly observed in the CCI monitoring results in Fig. 4 corresponds with loess material, which offers a perfect environment for the capture of renegade NGP due to its high porosity.

The monitoring results for images of the IP effect are not presented, as the monitoring images revealed negligible ϕ values along the entire experiments, similar to those resolved for the background

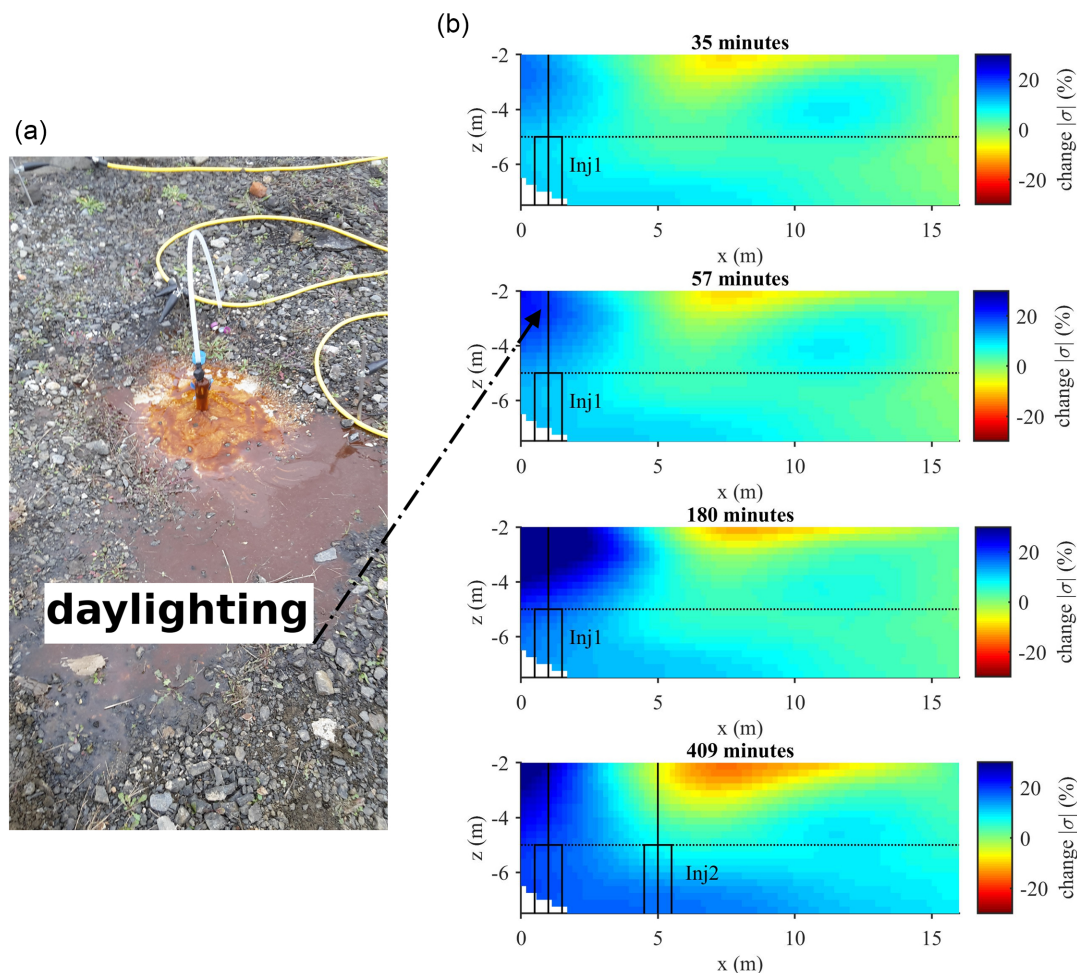


Figure 4. CCI monitoring results: (a) Daylighting observed in the vicinity of observation wells AW6-31 and AW6-32 after starting NGP delivery at 6.5 and 7 m bgl in Inj1. (b) CCI time-lapse imaging results for profile M1 in terms of the percentage change in $|\sigma|$ at different steps of the monitoring period. In Fig. 4(b), the dashed line indicates the depth to groundwater during the experiments, whereas the solid vertical lines show the position of the injection wells, with the rectangles indicating the injection areas.

Table 1. Fluid conductivity (σ_f) of NGP stock and injection suspension as well as the reference value of the groundwater and the Elbe River water. n.a.: not available.

Sample	Br ⁻ concentration	σ_f ($\mu\text{S cm}^{-1}$)	pH
NGP stock suspension	Stock suspension + ca. 1 g L ⁻¹ Br ⁻	4640	n.a.
NGP injection suspension (particle concentration ca. 20 g l ⁻¹)	Sample 1 + ca. 50 mg L ⁻¹ Br ⁻	1621	7.6
	Elbe River water	504	7.53
	On-site groundwater (containing BTEX)	1279	6.78

data (e.g. Fig. 2). The lack of an IP response following the injection can be explained by an increase in the fluid conductivity due to the injection of NGP suspension, characterized by a higher fluid conductivity than the one of the groundwater at the site (Table 1). A previous study in the laboratory revealed an initial increase in the polarization response with increasing fluid conductivity associated with sorption of ions into the Stern layer (Revil & Skold 2011). These authors also report a decrease in the polarization response at high salinity values for some samples, which they suggests may be due to membrane polarization. Based on the analysis of different samples, Weller *et al.* (2015) propose that the decrease in ion

mobility at high salinity values causes the decrease in the IP response. Based on the modelling of membrane polarization, Hördt *et al.* (2016), argue that a decrease in the zeta-potential needs also to be taken into account to explain the decrease in the IP response at high salinity values.

To better investigate the spatiotemporal changes in the electrical signature and their correlation with subsurface processes along the entire monitoring period, we present in Fig. 5 the values of representative geochemical parameters measured in water samples collected in different observation wells (AW6- 30, 31, 32, 34), as well as pixel values retrieved from the electrical images. Such pixel

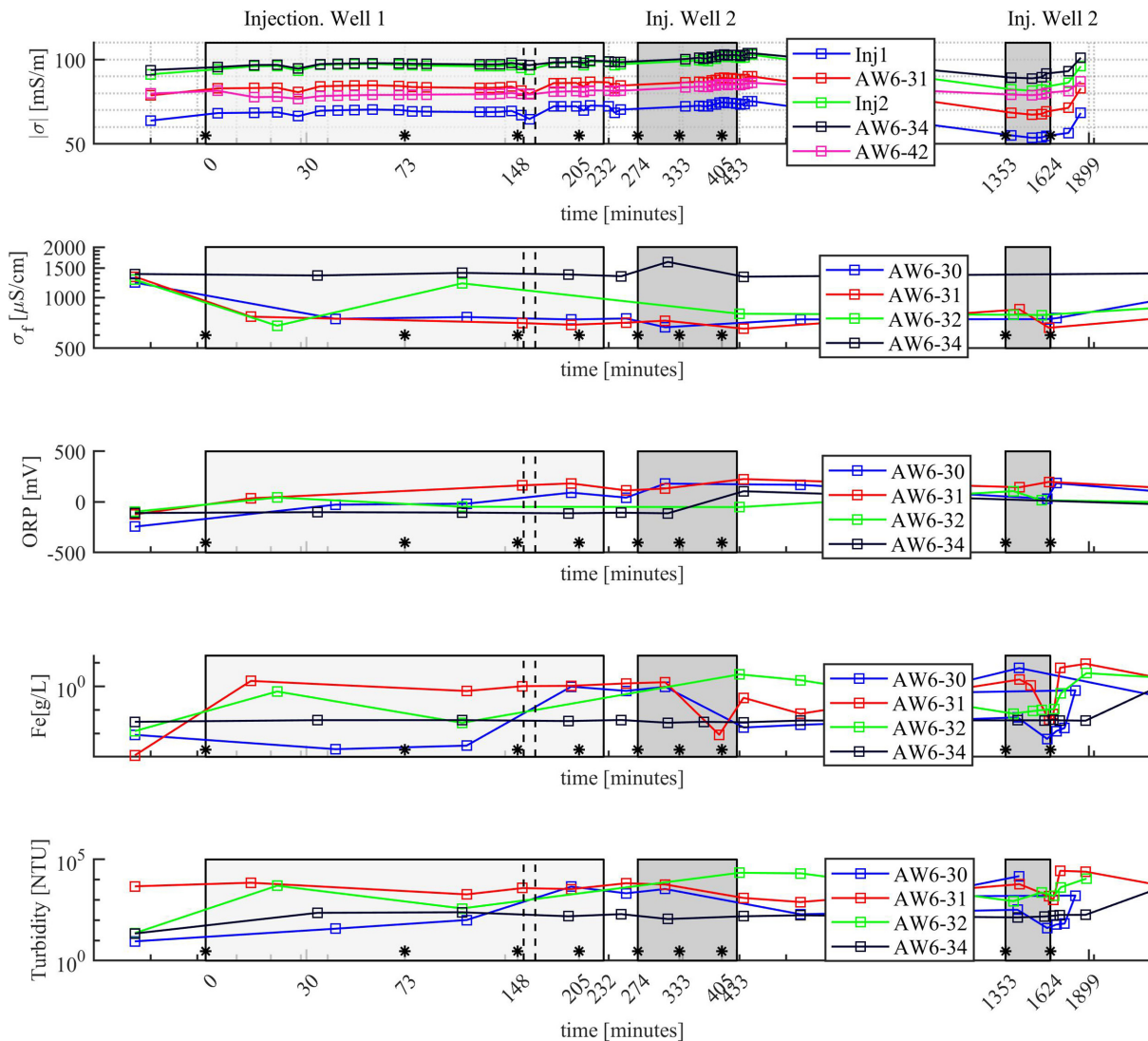


Figure 5. Geophysical and geochemical results for the monitoring period of the NGP injection. The electrical conductivity ($|\sigma|$) represents pixel values extracted from the electrical images between 5 and 7 m depth at the position of the injection points (Inj1 and Inj2) and observation wells (5a) along with the fluid electrical conductivity (5b), oxidation–reduction potential (5c), total iron content (5e) and turbidity (5e) measured in water samples. The grey-shaded zones represent the injection periods at each injection well. The vertical dashed line indicates the time of the first two daylighting events reported. The symbols (*) represent the beginning of injections at depths of 5, 5.5, 6 and 7.5 m at Inj1, as well as at depths of 5, 5.5 and 6 m depth at Inj2.

values represent the median $|\sigma|$ values between 5 and 8 m depth at the position of the observation wells and the first injection point (Inj1). The injection periods at Inj1 and Inj2 are indicated by the grey shaded areas. The blank area in Fig. 5 (between ~500 min and 24 hr) is due to overnight breaks, during which it was not possible to collect geophysical or geochemical data.

Fig. 5 reveals a slight increase in $|\sigma|$ during the injection period for most of the retrieved pixels, with the exception of observation well AW6-42. After finishing the injection in Inj1, Fig. 5 reveals a drop in the $|\sigma|$ values, which bounce back once the injection starts in Inj2. However, a more significant decrease in $|\sigma|$ is observed during the overnight break, which evidences a change from 75 mS m^{-1} to 55 mS m^{-1} for pixels extracted at the position of Inj1. Similar variations in $|\sigma|$ are also observed for the rest of the extracted pixels, with the exception of observation well AW6-42. This well is located 15 m down gradient from the injection point, where only a slight change in $|\sigma|$ is observed, suggesting that only minimal amounts of NGP suspension were transported to such distance during the first

injection day. In agreement with those observations, NGP injections at the second point (Inj2) are also related to a slight increase in $|\sigma|$.

Opposite to the trend observed in $|\sigma|$ values, *in-situ* measurements of σ_f revealed a significant decrease (~45 per cent) directly after starting the injection for water samples collected in observation wells close to the injection point (AW6-31 and 32). Such observation is not easy to explain, considering that the fluid conductivity of the injected NGP suspension is higher than the one of the groundwater (Table 1). Instead, we hypothesize that the mixing of shallow and deeper groundwater due to the NGP injection concurrent with the pumping in the observation wells causes the observed decrease in σ_f . This hypothesis is consistent with the lack of changes in observation wells located down gradient (e.g. AW6-42) the injection points.

Due to the high reactivity of the particles, Oxidation-Reduction Potential (ORP) measurements can be used as a proxy to monitor particle delivery (see Shi *et al.* 2011 and references therein). Consistently, during our experiments subsurface enrichment with NGP

can be evidenced by the continuous increase in ORP values in observation wells AW6-30 and AW6-31 along the entire monitoring period (Fig. 5c). Yet, such trend is followed by a decrease to pre-injection values after ~30 min, which is the time at which fracking can be inferred from the CCI results. Hence, ORP variations are also consistent to the interpretation of the electrical images.

Distinctive to such trend, ORP measurements reported 15 m down gradient from the injection point (AW6-42) reveal negligible changes over the first 450 min of the NGP amendment. Nevertheless, samples collected after concluding injections at 5.5 m depth at Inj2 show an increase in the ORP values, suggesting that some NGP suspension might have been transported 15 m after 8 hr. Such observation is also consistent with the slight increase in $|\sigma|$ resolved through the electrical monitoring. However, the negligible changes in Fe_{tot} indicate that no NGP were transported to such distances and the observed changes may be related only to the accumulation of the stabilizing solution of humic acids.

Measurements of the Fe_{tot} (Fig. 5d) can be used in the interpretation of CCI results and to evaluate the delivery of NGP. As expected, following the first injection, iron concentration increases in the observation wells near the injection (AW6-31 and AW6-32). Accordingly, Fe_{tot} also increases in the observation well located up gradient the injection point (AW6-30) after the reported daylighting (~160 min after starting the first injection). However, the Fe_{tot} concentration in AW6-30 dropped significantly before finishing the first injection period. Such observation in well AW6-30 is consistent with the turbidity measurements (another proxy to assess the presence of NP in water samples, see Shi *et al.* 2015), which also reveal an increase concurrent with the reported daylighting (Fig. 5e). However, turbidity bouncing back to initial values after starting the second NGP amendment (in Inj2) can be related to problems with the sampling or deviations in the particles due to fractures created during the first injection (e.g. daylighting). Additionally, turbidity measurements reveal an initial increase in AW6-30 and AW6-32 after starting the injections; yet, this is followed by fluctuations poorly correlated with the NGP injections. Furthermore, turbidity values show negligible changes in samples collected in observation wells AW6-31 (directly next to the injection well) and AW6-34 (15 m downgradient), suggesting that particles were mainly delivered to fractures connecting the injection point to the surface. Both, temperature and pH revealed only negligible changes along the monitoring period, with values around a mean value of 13 °C and a quasi-neutral pH of 7.2 (data not shown).

3.5 The lack of sensitivity of induced polarization images following the injection of nano-goethite particles

As an induced-polarization method, CCI is known to be highly sensitive to metallic particles in the subsurface (e.g. Pelton *et al.* 1978; Ward 1990). The large polarization magnitude of the underlying electrode-polarization process is mainly caused by the high electrical conductivity of the particles compared to the one of the surrounding electrolyte solution (e.g. Wong 1979). Although it is an iron-bearing mineral, goethite is a semiconductor and its relatively large band gap (2.1 eV) results in a very low electrical conductivity (approx. $10\text{--}3\ \mu\text{S cm}^{-1}$) at room temperature (Cornell & Schwertmann 2003). Thus, the polarization response of goethite cannot be attributed to electrode polarization. More likely, it is caused by the polarization of the electrical double layer covering the charged surface of non-conducting particles as discussed by Abdel Aal *et al.* (2014). A non-zero charge at the surface of goethite particles is

well documented (e.g. Cornell & Schwertmann 2003; and references therein), such that it is straightforward to assume the action of a Stern-layer (e.g. Leroy *et al.* 2008) or diffuse-layer (e.g. Fixman 1980; Shilov *et al.* 2001) polarization process around the goethite particles. Laboratory IP measurements on goethite indicate a low (Huisman *et al.* 2014) or negligible low-frequency polarization (Olhoeft 1982; Abdel Aal *et al.* 2014) of goethite surfaces compared to those on conductive minerals (e.g. pyrite, magnetite, graphite). Thus, the absence of a characteristic CC signature of the NGP at frequencies around 1 Hz in our experiments is in perfect agreement with both theoretical considerations and earlier experimental findings.

A possible technical means to increase the phase response of the particles or particle aggregates would be to use (much) higher frequencies: Laboratory measurements with goethite nanoparticles conducted by Huisman *et al.* (2014) found a measurable increase of the imaginary part of the conductivity around 1 kHz and for comparable particle concentrations. However, in field applications, inductive and capacitive coupling effects generally mask the IP response and render the interpretation of high-frequency CCI data challenging (e.g. Pelton *et al.* 1978; Flores Orozco *et al.* 2013, 2018a and references therein). In particular, inductive coupling effects arise due to the conduction of current along the cables connecting the measuring instrument and the electrodes, which are proportional to the bulk conductivity of the subsurface, the acquisition frequency and the square of the cable length (Hollof *et al.* 1974). Hence, collection of high-frequency IP data in areas characterized by high electrical conductivity (e.g. mature hydrocarbon plumes) or by the injection of NP dispersions with high fluid conductivity may be challenging due to contamination of the IP data by inductive coupling. Clearly, the problem will increase with increasing the depth of investigation, which requires the collection of data with longer cables. A recommendation for future campaigns would be to find a trade-off between signal strength and adverse high-frequency effects in order to maximize the information on NPG in the phase response. Accordingly, the development of dispersion solutions characterized by low fluid conductivity could also be beneficial to improve the sensitivity of the CCI method for the characterization of nanoparticles injections. The collection of IP data over a long time-span might also be important for further studies to assess long-term variations in the signatures associated with the agglomeration of the particles, which may result in larger particle sizes and measurable IP signatures at the low frequencies. Moreover, further changes in the IP signatures might also be related to chemical transformations of the contaminant (e.g. Revil *et al.* 2011) or the accumulation of iron-minerals (Flores Orozco *et al.* 2011, 2013; Abdel Aal *et al.* 2014) due to the expected stimulation of microbial activity (e.g. Braunschweig *et al.* 2013).

3.6 The potential of geophysical monitoring to reveal pore-space clogging and to guide geochemical sampling

To facilitate the quantitative interpretation of changes in the electrical conductivity along the monitoring period, we present in Fig. 6 the response of the same extracted pixels presented in Fig. 5, but plotted as the change in the $|\sigma|$ from baseline.

Fig. 6 clearly reveals a significant decrease in the bulk electrical conductivity concurrent with the daylighting reported in wells AW6-31 and 32 (indicated by the dashed lines). A straightforward explanation of such sudden drop can be given by the pore-space clogging due to the accumulation and sedimentation

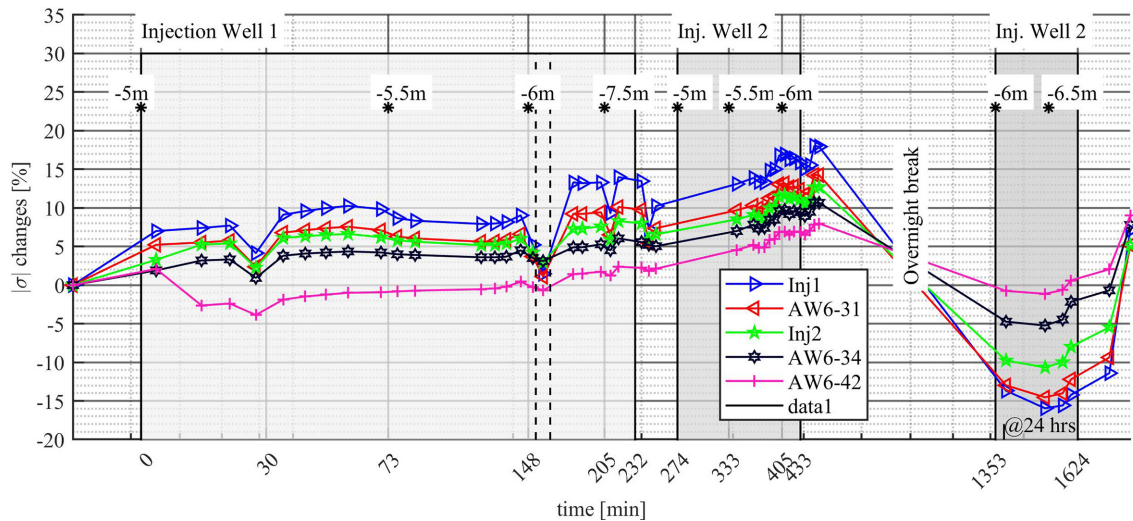


Figure 6. Percentage changes in the electrical conductivity ($|\sigma|$) for the inversion results between the baseline and monitoring measurements. Electrical parameters represent the median for pixel values extracted from the electrical images between 5.5 and 7 m depth at the position of the injection and observation wells. The vertical dashed line represents the time at which the first daylighting was observed in well AW6-30. The grey polygons represent the delivery periods in Inj1 and Inj2.

of NGP near the injection point. The interaction between NP and the corresponding agglomeration and loss of mobility over time have been largely documented, including coated iron oxides (e.g. Vecchia *et al.* 2009; Tiraferri *et al.* 2017); furthermore, as discussed by Luna *et al.* (2015), long injections commonly result in the sedimentation of the particles. Hence, a two-step process can explain the $|\sigma|$ patterns observed in Fig. 6: (1) first a decrease in porosity (and $|\sigma|$) due to the clogging of the pore space; followed by (2) an increase in the porosity (and $|\sigma|$) due to fracturing and the filling of the associated fractures with NGP solution and groundwater.

To better illustrate this, we can look in detail at the changes in $|\sigma|$ accompanying the first injection (i.e. at Inj1 and 5 m depth). Here, the NGP delivery was performed at low pressure (5–6 bar) and over a long injection time (>60 min), which are conditions promoting particle sedimentation (e.g. Luna *et al.* 2015). Accordingly, the observed decrease in $|\sigma|$ values (at ~ 28 min), is most likely an indication of pore clogging. Hence, the further delivery of NGP suspension resulted in an increase in pore-pressure and the development of fracturing, which can be evidenced in the geophysical imaging by the rapid increase in $|\sigma|$, for instance at ~ 35 min. Hence, the slight decrease in the electrical conductivity observed during the injections at 5.5 m depth can be related to clogging of both the pores and the previously created fractures. Consequently, further injections at 6 m depth, and related plugging of the pore space, resulted in the strong decrease in $|\sigma|$ observed at ~ 160 min, which also led to the further development of the fractures and the daylighting events.

While geochemical analysis cannot help to validate the interpretation of the electrical images, the presence of iron in the solution flowing to the surface, clearly indicates that the injected solution was delivered through fractures to observations wells and the surface. Moreover, the increase in the $|\sigma|$ values in the unsaturated zone close to the injections wells observed in Fig. 4 also supports our interpretation. Here, such anomalies suggest that NGP and/or the dispersion solution found preferential flow paths leading to their accumulation in the unsaturated loss materials.

Following the overnight break, CCI results reveal a significant decrease in $|\sigma|$, even below baseline values. In particular, pixel values close to Inj1 (e.g. AW6-31) show a decrease of 16 per cent in comparison to baseline values and about 26 per cent when compared to the measurement before the overnight break. A first explanation for this conductivity drop can be the degradation of the humic acids coating the NGP particles, and, thus, pore clogging due to particle aggregation. Yet, no hydro-geochemical data are available to sustain this possible interpretation. Nonetheless, our results suggest that CCI may be a suitable method to evaluate changes in porosity following the subsurface enrichment with NP, either associated to fracturing developed during the injection or pore clogging after finishing the delivery of the slurry.

While geochemical data are available only in ca. 12 samples for each observation well, CCI data sets were collected every 7 min allowing tracking the fate of NP in 54 time steps. In addition to that, not all observation wells were sampled along the 12 geochemical time lapses, for instance, observations wells up and down gradient (AW6-30 and -34, respectively) were sampled only 30 min after starting the injection, and then only every 60 min. Moreover, clogging in the tubing of the monitoring wells affected by the daylighting (AW6-32) impeded the collection of water samples, further limiting the resolution of the geochemical monitoring. CCI may overcome some of these limitations in monitoring applications, especially regarding the spatial and temporal resolution.

Although our results show that CCI is a promising method for the monitoring of NP injections, geochemical monitoring is still critical to permit an adequate interpretation of the electrical signatures. We suggest that following experiments consider adjusting the geochemical sampling in order to take into account the geophysical response. Hence, a coupled geochemical–geophysical monitoring could improve the quantitative interpretation of CCI images and permit to improve the efficiency of the remediation method by providing real-time information.

Further information is needed to evaluate the uncertainty in geochemical data. The geochemical variations observed in well AW6-34 illustrate the problem: geochemical monitoring revealed no changes in σ_f , Fe_{tot} and turbidity, suggesting that NGP were not

transported 15 m down gradient the injection points. However, ORP measurements revealed an increase in AW6-34 after starting the first injection (~480 min), which are also consistent with a slight increase in $|\sigma|$ in that area after concluding the NGP amendment at 6 m depth in Inj2 (~453 min after starting the first injection as presented in Fig. 6). We explain our observations as the effect of the injected solution consisting only of humic acids (causing the increase in $|\sigma|$ and ORP), but negligible NGP concentrations. On the one hand, the lack of changes in the σ_f seems to challenge such interpretation. On the other hand, well AW6-34 is fully screened between 6 and 8 m depth, which might induce the mixing of groundwater from different depths and distances during the sampling. Hence, the discrepancy observed between $|\sigma|$ and σ_f might be related to mixed water samples, which may also bias other geochemical parameters such as Fe_{tot} .

4 CONCLUSIONS

We presented the first field-scale application of the CCI method to monitor subsurface processes accompanying the injection of nanoparticles, in particular NGP. Our imaging results permitted to identify clogging of the pore space, that is, a decrease of hydraulic conductivity at the injection point. The continuous injection resulted in the unintended development of preferential flow paths and the delivery of NGP in areas away of the target, leading to an overall decrease in the efficiency of the remediation technique.

Spatial variations in the electrical conductivity $|\sigma|$ for baseline images revealed a good correlation with the lithological units. The IP effect, a measure of the capacitive properties, revealed only a weak response, which can be explained by the occurrence of the contaminant in free-phase (displacing groundwater) and the high fluid conductivity of groundwater; the latter possibly being a result of the release of carbonic acids as metabolic products of hydrocarbon-degrading organisms, a well-documented process in mature plumes.

CCI monitoring results revealed four consecutive steps in the electrical signatures governed by the delivery and transport of NGP suspension, namely: (i) an increase in the electrical conductivity ($|\sigma|$) associated to the subsurface enrichment of the NGP solution, characterized by a fluid conductivity 26 per cent higher than that of groundwater; (ii) a sudden drop in $|\sigma|$, likely associated to pore clogging and permeability loss; which is followed by (iii) an increase in $|\sigma|$, accompanying daylighting events, likely indicating the occurrence of fracturing and the development of secondary porosity and (iv) an important decrease of ~14 per cent below baseline values in $|\sigma|$ during the overnight brake, which can be explained by clogging due to changes in the surface properties of injected NGP. Our study demonstrates that geophysical monitoring data—if incorporated into the design of NP injections—offers unique possibilities to improve the efficiency of groundwater remediation measures. On the one hand, CCI results for background data demonstrate that pre-injection information could be used in the design of the injection strategy (e.g. to avoid injection to low hydraulic conductive areas). On the other hand, monitoring results can be used to gain information in quasi real-time to assess clogging of the pore space; thus, permitting re-locating the NP injection and a more effective delivery of particles. Although CCI monitoring provides information with enhanced spatial and temporal resolution, the complete advantages of the method cannot be fully exploited without additional geochemical information for the quantitative interpretation of the results. Hence, we suggest that the geochemical sampling should be performed taking into account real-time CCI results.

ACKNOWLEDGEMENTS

This material is partially based upon work supported by the Austrian Federal Ministry of Education, Science and Research (BMBWF) through the POTHAL project (Development of geophysical exploration methods for the characterization of mine-tailings towards exploitation). The NanoRem project has received funding from the European Union's Seventh Framework Programme for research, technological development and demonstration under grant agreement no 309517. The authors would like to thank AQUATEST a.s., CZ, for providing the information about the investigated site, as well as the geochemical data prior to the NGP injection. The authors like to thank Doris Schmid for fieldwork and analysis of geochemical data.

REFERENCES

- Abdel Aal, G., Atekwana, E.A. & Werkema, D.D., Jr, 2017. Complex conductivity response to silver nanoparticles in partially saturated sand columns, *J. appl. Geophys.*, **137**, 73–81.
- Abdel Aal, G.Z., Atekwana, E.A. & Revil, A., 2014. Geophysical signatures of disseminated iron minerals: a proxy for understanding subsurface biophysicochemical processes, *J. geophys. Res.*, **119**(9), 1831–1849.
- Abdel Aal, G.Z., Atekwana, E.A., Slater, L.D. & Atekwana, E.A., 2004. Effects of microbial processes on electrolytic and interfacial electrical properties of unconsolidated sediments, *Geophys. Res. Lett.*, **31**(12).
- Abdel Aal, G.Z., Slater, L.D. & Atekwana, E.A., 2006. Induced-polarization measurements on unconsolidated sediments from a site of active hydrocarbon biodegradation: Geophysics, **71**(2), H13–H24.
- Adeleye, A.S., Conway, J.R., Garner, K., Huang, Y., Su, Y. & Keller, A.A., 2016. Engineered nanomaterials for water treatment and remediation: costs, benefits, and applicability, *Chem. Eng. J.*, **286**, 640–662.
- Atekwana, E.A. & Atekwana, E.A., 2010. Geophysical signatures of microbial activity at hydrocarbon contaminated sites: a review, *Surv. Geophys.*, **31**, 247–283.
- Bardos, P., Merly, C., Kvapil, P. & Koschitzky, H.P., 2018. Status of nanoremediation and its potential for future deployment: risk-benefit and benchmarking appraisals, *Remediation J.*, **28**(3), 43–56.
- Bhattacharjee, S. & Ghoshal, S., 2018. Optimal design of sulfidated nanoscale zerovalent iron for enhanced trichloroethene degradation, *Environ. Sci. Technol.*, **52**(19), 11 078–11 086.
- Bianco, C., Higueta, J.E.P., Tosco, T., Tiraferri, A. & Sethi, R., 2017. Controlled deposition of particles in porous media for effective aquifer nanoremediation, *Sci. Rep.*, **7**(1), 12992.
- Binley, A., Keery, J., Slater, L., Barrash, W. & Cardiff, M., 2016. The hydrogeologic information in cross-borehole complex conductivity data from an unconsolidated conglomeratic sedimentary aquifer: Cross-borehole complex conductivity, *Geophysics*, **81**(6), E409–E421.
- Binley, A. & Kemna, A., 2005. DC resistivity and induced polarization methods, in *Hydrogeophysics*, pp. 129–156, eds Rubin, Y. & Hubbard, S.S., Springer, Dordrecht.
- Bosch, J., Heister, K., Hofmann, T. & Meckenstock, R.U., 2010. Nanosized iron oxide colloids strongly enhance microbial iron reduction, *Appl. Environ. Microbiol.*, **76**(1), 184–189.
- Braunschweig, J., Bosch, J. & Meckenstock, R.U., 2013. Iron oxide nanoparticles in geomicrobiology: from biogeochemistry to bioremediation, *New Biotechnol.*, **30**(6), 793–802.
- Bücker, M., Flores Orozco, A., Hördt, A. & Kemna, A., 2017. An analytical membrane-polarization model to predict the complex conductivity signature of immiscible liquid hydrocarbon contaminants, *Near Surf. Geophys.*, **15**(6), 547–562.
- Bücker, M., Flores Orozco, A. & Kemna, A., 2018. Electro-chemical polarization around metallic particles—Part 1: the role of diffuse-layer and volume-diffusion relaxation, *Geophysics*, **83**(4), 1–53.
- Bücker, M. & Hördt, A., 2013. Long and short narrow pore models for membrane polarization, *Geophysics*, **78**(6), E299–E314.

- Cassiani, G., Kemna, A., Villa, A. & Zimmermann, E., 2009. Spectral induced polarization for the characterization of free-phase hydrocarbon contamination of sediments with low clay content, *Near Surf. Geophys.*, **7**, 547–562.
- Cassiani, G. et al., 2014. Non-invasive characterization of the Trecate (Italy) crude-oil contaminated site: links between contamination and geophysical signals: Environmental Science and Pollution Research, Special Issue on “New approaches for low-invasive contaminated site characterization, monitoring and modelling”, *Environ. Sci. Pollut. Res.*, **21**, 8914–8931.
- Cassidy, D.P., Werkema Jr, D.D., Sauck, W., Atekwana, E., Rossbach, S. & Duris, J., 2001. The effects of LNAPL biodegradation products on electrical conductivity measurements, *Journal of Environmental and Engineering Geophysics*, **6**(1), 47–52.
- Caterina, D., Flores Orozco, A. & Nguyen, F., 2017. Long-term ERT monitoring of biogeochemical changes of an aged hydrocarbon contamination, *J. Contam. Hydrol.*, **201**, 19–29.
- Chen, C.F., Binh, N.T., Chen, C.W. & Dong, C.D., 2015. Removal of polycyclic aromatic hydrocarbons from sediments using sodium persulfate activated by temperature and nanoscale zero-valent iron, *J. Air Waste Manage. Assoc.*, **65**(4), 375–383.
- Chen, J., Hubbard, S.S., Williams, K.H., Flores Orozco, A. & Kemna, A., 2012. Estimating the spatiotemporal distribution of geochemical parameters associated with biostimulation using spectral induced polarization data and hierarchical Bayesian models, *Water Resour. Res.*, **48**(5), doi:10.1029/2011WR010992.
- Cornell, R.M. & Schwertmann, U., 2003. *The Iron Oxides: Structure, Properties, Reactions, Occurrences and Uses*, John Wiley & Sons, Hoboken, NJ.
- Dahlin, T. & Zhou, B., 2006. Multiple-gradient array measurements for multichannel 2D resistivity imaging: near surface geophysics, **4**(2), 113–123.
- Deceuster, J. & Kaufmann, O., 2012. Improving the delineation of hydrocarbon impacted soils and water through induced polarization (IP) tomographies: a field study at an industrial waste land, *J. Contam. Hydrol.*, **136**, 25–42.
- Deng, Y., Shi, X., Revil, A., Wu, J. & Ghorbani, A., 2018. Complex conductivity of oil-contaminated clayey soils, *J. Hydrol.*, **561**, 930–942.
- Estella, A., Atekwana & Lee, D. Slater, 2009. Biogeophysics: A new frontier in Earth science research, *Reviews of Geophysics*, **47**(4), 30.
- Fixman, M., 1980. Charged macromolecules in external fields. I. The sphere, *J. Chem. Phys.*, **72**(9), 5177–5186.
- Flores Orozco, A., Bückner, M., Steiner, M. & Malet, J.P., 2018a. Complex-conductivity imaging for the understanding of landslide architecture, *Eng. Geol.*, **243**, 241–252.
- Flores Orozco, A., Gallistl, J., Bückner, M. & Williams, K.H., 2018b. Decay curve analysis for data error quantification in time-domain induced polarization imaging, *Geophysics*, **83**(2), E75–E86.
- Flores Orozco, A., Kemna, A., Binley, A. & Cassiani, G., 2019. Analysis of time-lapse data error in complex conductivity imaging to alleviate anthropogenic noise for site characterization, *Geophysics*, **84**(2), B181–B193.
- Flores Orozco, A., Kemna, A., Oberdörster, C., Zschornack, L., Leven, C., Dietrich, P. & Weiss, H., 2012a. Delineation of subsurface hydrocarbon contamination at a former hydrogenation plant using spectral induced polarization imaging, *J. Contam. Hydrol.*, **136**, 131–144.
- Flores Orozco, A., Kemna, A. & Zimmermann, E., 2012b. Data error quantification in spectral induced polarization imaging, *Geophysics*, **77**(3), E227–E237.
- Flores Orozco, A., Velimirovic, M., Tosco, T., Kemna, A., Sapion, H., Klaas, N., Sethi, R. & Bastiaens, L., 2015. Monitoring the injection of microscale zerovalent iron particles for groundwater remediation by means of complex electrical conductivity imaging, *Environ. Sci. Technol.*, **49**(9), 5593–5600.
- Flores Orozco, A., Williams, K.H. & Kemna, A., 2013. Time-lapse spectral induced polarization imaging of stimulated uranium bioremediation, *Near Surf. Geophys.*, **11**(5), 531–544.
- Flores Orozco, A., Williams, K.H., Long, P.E., Hubbard, S.S. & Kemna, A., 2011. Using complex resistivity imaging to infer biogeochemical processes associated with bioremediation of a uranium-contaminated aquifer, *J. geophys. Res.*, **116**, G03001, doi:10.1029/2010JG001591.
- Gallistl, J., Weigand, M., Stumvoll, M., Ottowitz, D., Glade, T. & Flores Orozco, A., 2018. Delineation of subsurface variability in clay-rich landslides through spectral induced polarization imaging and electromagnetic methods, *Eng. Geol.*, **245**, 292–308.
- Grieger, K.D., Fjordbøge, A., Hartmann, N.B., Eriksson, E., Bjerg, P.L. & Baun, A., 2010. Environmental benefits and risks of zero-valent iron nanoparticles (nZVI) for in situ remediation: risk mitigation or trade-off? *J. Contam. Hydrol.*, **118**(3–4), 165–183.
- Hallof, P.G., 1974. The IP phase measurement and inductive coupling, *Geophysics*, **39**(5), 650–665.
- Heenan, J. et al., 2014. Electrical resistivity imaging for long-term autonomous monitoring of hydrocarbon degradation: Lessons from the Deepwater Horizon oil spill, *Geophysics*, **80**(1), B1–B11.
- Hosseini, S.M. & Tosco, T., 2015. Integrating NZVI and carbon substrates in a non-pumping reactive wells array for the remediation of a nitrate contaminated aquifer, *J. Contam. Hydrol.*, **179**, 182–195.
- Hua, M., Zhang, S., Pan, B., Zhang, W., Lv, L. & Zhang, Q., 2012. Heavy metal removal from water/wastewater by nanosized metal oxides: a review, *J. Hazard. Mater.*, **211**, 317–331.
- Huisman, J.A., Moradi, S., Zimmermann, E., Bosch, J. & Vereecken, H., 2014. Spectral induced polarization of goethite nanoparticles, i AGU Fall Meeting Abstracts 2014, San-Francisco.
- Huling, S.G., Pivetz, B. & Stransky, R., 2002. Terminal electron acceptor mass balance: light nonaqueous phase liquids and natural attenuation, *J. Environ. Eng.*, **128**, 246–252.
- Hördt, A., Bairlein, K., Bielefeld, A., Bückner, M., Kuhn, E., Nordsiek, S. & Stebner, H., 2016. The dependence of induced polarization on fluid salinity and pH, studied with an extended model of membrane polarization, *J. appl. Geophys.*, **135**, 408–417.
- Hördt, A., Bairlein, K., Bückner, M. & Stebner, H., 2017. Geometrical constraints for membrane polarization, *Near Surf. Geophys.*, **15**(6), 579–592.
- Johansson, S., Fiandaca, G. & Dahlin, T., 2015. Influence of non-aqueous phase liquid configuration on induced polarization parameters: Conceptual models applied to a time-domain field case study, *J. appl. Geophys.*, **123**, 295–309.
- Joyce, R.A., Glaser, D.R., II, Werkema, D.D., Jr & Atekwana, E.A., 2012. Spectral induced polarization response to nanoparticles in a saturated sand matrix, *J. appl. Geophys.*, **77**, 63–71.
- Karn, B., Kuiken, T. & Otto, M., 2009. Nanotechnology and in situ remediation: a review of the benefits and potential risks, *Environ. Health Perspect.*, **117**(12), 1813, doi:10.1289/ehp.0900793.
- Kemna, A., 2000. *Tomographic Inversion of Complex Resistivity: Theory and Application*, Der Andere Verlag, Osnabrück.
- Kemna, A. et al., 2012. An overview of the spectral induced polarization method for near-surface applications, *Near Surf. Geophys.*, **10**(6), 453–468.
- Lei, C., Sun, Y., Tsang, D.C. & Lin, D., 2018. Environmental transformations and ecological effects of iron-based nanoparticles, *Environ. Pollut.*, **232**, 10–30.
- Leroy, P., Revil, A., Kemna, A., Cosenza, P. & Ghorbani, A., 2008. Complex conductivity of water-saturated packs of glass beads, *Journal of Colloid and Interface Science*, **321**(1), 103–117.
- Lesparre, N., Nguyen, F., Kemna, A., Robert, T., Hermans, T., Daoudi, M. & Flores Orozco, A., 2017. A new approach for time-lapse data weighting in ERT, *Geophysics*, **82**(6), 325–E333.
- Luna, M. et al., 2015. Pressure-controlled injection of guar gum stabilized microscale zerovalent iron for groundwater remediation, *J. Contam. Hydrol.*, **181**, 46–58.
- Maineult, A., Jougnot, D. & Revil, A., 2018. Variations of petrophysical properties and spectral induced polarization in response to drainage and imbibition: a study on a correlated random tube network, *Geophys. J. Int.*, **212**(2), 1398–1411.
- Marshall, D.J. & Madden, T.R., 1959. Induced polarization, a study of its causes, *Geophysics*, **24**(4), 790–816.

- Meckenstock, R.U. & Bosch, J., 2014. Method for the degradation of pollutants in water and/or soil, United States patent.
- Mellage, A., Holmes, A.B., Linley, S., Vallée, L., Rezanezhad, F., Thomson, N., Gu, F.X. & Van Cappellen, P., 2018. Sensing coated iron-oxide nanoparticles with spectral induced polarization (SIP): experiments in natural sand packed flow-through columns, *Environ. Sci. Technol.*, **52**, 14256–14265.
- Misra, S., Torres-Verdín, C., Revil, A., Rasmus, J. & Homan, D., 2016. Interfacial polarization of disseminated conductive minerals in absence of redox-active species. Part 1: mechanistic model and validation, *Geophysics*, **81**(2), E139–E157.
- Mueller, N.C., Braun, J., Bruns, J., Cerník, M., Rissing, P., Rickerby, D. & Nowack, B., 2012. Application of nanoscale zero valent iron (NZVI) for groundwater remediation in Europe, *Environ. Sci. Pollut. Res.*, **19**(2), 550–558.
- NanoRem Bulletin 8- NanoRem Pilot Site – Spolchemie II, Czech Republic: Remediation of BTEX Compounds Using Nano-Goethite. Available at: www.nanorem.eu, Access 12 June 2019.
- Nathanail, C.P., Gillett, A., McCaffrey, C., Nathanail, J. & Ogden, R., 2016. A preliminary risk assessment protocol for renegade nanoparticles deployed during nanoremediation, *Remediation J.*, **26**(3), 95–108.
- Ntarlagiannis, D., Ustra, A., Kessouri, P. & Flores Orozco, A., 2018. The untapped potential of the induced polarization method: characterization and monitoring of hydrocarbon contamination in soils, *FastTIMES*, **23**(4), 64–75.
- Okay, G., Cosenza, P., Ghorbani, A., Camerlynck, C., Cabrera, J., Florsch, N. & Revil, A., 2013. Characterization of macroscopic heterogeneities in clay-rocks using induced polarization: Field tests at the experimental underground research laboratory of Tournemire (Aveyron, France), *Geophys. Prospect.*, **61**, 134–152.
- Olhoeft, G.R., 1982. Warburg impedances at single water-mineral interfaces, in *SEG Technical Program Expanded Abstracts 1982*, pp. 516–518, Society of Exploration Geophysicists, Tulsa, OK.
- Olhoeft, G.R., 1985. Low-frequency electrical-properties, *Geophysics*, **50**, 2492–2503.
- Patil, S.S., Shedbalkar, U.U., Truskewycz, A., Chopade, B.A. & Ball, A.S., 2016. Nanoparticles for environmental clean-up: a review of potential risks and emerging solutions, *Environ. Technol. Innov.*, **5**, 10–21.
- Pelton, W.H., Ward, S.H., Hallof, P.G., Sill, W.R. & Nelson, P.H., 1978. Mineral discrimination and removal of inductive coupling with multifrequency IP, *Geophysics*, **43**, 588–609.
- Revil, A., Abdel Aal, G.Z., Atekwana, A., Mao, D. & Florsch, N., 2015. Induced polarization response of porous media with metallic particles — Part 2. Comparison with a broad database of experimental data, *Geophysics*, **80**(5), D539–D552.
- Revil, A., Atekwana, E., Zhang, C., Jardani, A. & Smith, S., 2012. A new model for the spectral induced polarization signature of bacterial growth in porous media, *Water Resour. Res.*, **48**, W09545, doi:10.1029/2012WR011965.
- Revil, A. & Florsch, N., 2010. Determination of permeability from spectral induced polarization data in granular media, *Geophys. J. Int.*, **181**, 1480–1498.
- Revil, A., Schmutz, M. & Batzle, M.L., 2011. Influence of oil wettability upon spectral induced polarization of oil-bearing sands, *Geophysics*, **76**(5), A31–A36.
- Revil, A. & Skold, M., 2011. Salinity dependence of spectral induced polarization in sands and sandstones, *Geophys. J. Int.*, **187**(2), 813–824.
- Revil, A. *et al.*, 2017. Complex conductivity of soils, *Water Resour. Res.*, **53**(8), 7121–7147.
- Saneiyani, S., Ntarlagiannis, D., Ohan, J., Lee, J., Colwell, F. & Burns, S., 2019. Induced polarization as a monitoring tool for in-situ microbial induced carbonate precipitation (MICP) processes, *Ecol. Eng.*, **127**, 36–47.
- Schirmer, M. *et al.*, 2006. Natural attenuation research at the contaminated megasite Zeitz, *J. Hydrol.*, **328**, 393–407.
- Schmid, D., Micic, V., Laumann, S. & Hofmann, T., 2015. Measuring the reactivity of commercially available zero-valent iron nanoparticles used for environmental remediation with iopromide, *J. Contam. Hydrol.*, **181**, 36–45.
- Schmutz, M., Revil, A., Vaudelet, P., Batzle, M., Femenía Viñao, P. & Werkema, D., 2010. Influence of oil saturation upon spectral induced polarization of oil bearing sands, *Geophys. J. Int.*, **183**, 211–224.
- Schurr, J.M., 1964. On the theory of the dielectric dispersion of spherical colloidal particles in electrolyte solution1, *The Journal of Physical Chemistry*, **68**(9), 2407–2413.
- Schwartz, N., Huisman, J.A. & Furman, A., 2012. The effect of NAPL on the electrical properties of unsaturated porous media, *Geophys. J. Int.*, **188**(3), 1007–1011.
- Schwarz, G., 1962. A theory of the low-frequency dielectric dispersion of colloidal particles in electrolyte solution1, 2, *J. Phys. Chem.*, **66**(12), 2636–2642.
- Shefer, I., Schwartz, N. & Furman, A., 2013. The effect of free-phase NAPL on the spectral induced polarization signature of variably saturated soil, *Water Resour. Res.*, **49**(10), 6229–6237.
- Shilov, V.N., Delgado, A.V., Gonzalez-Caballero, F. & Grosse, C., 2001. Thin double layer theory of the wide-frequency range dielectric dispersion of suspensions of non-conducting spherical particles including surface conductivity of the stagnant layer, *Colloids Surf. A*, **192**(1–3), 253–265.
- Shi, Z., Fan, D., Johnson, R.L., Tratnyek, P.G., Nurmi, J.T., Wu, Y. & Williams, K.H., 2015. Methods for characterizing the fate and effects of nano zerovalent iron during groundwater remediation, *J. Contam. Hydrol.*, **181**, 17–35.
- Shi, Z., Nurmi, J.T. & Tratnyek, P.G., 2011. Effects of nano zero-valent iron on oxidation–reduction potential, *Environ. Sci. Technol.*, **45**(4), 1586–1592.
- Slater, L., 2007. Near surface electrical characterization of hydraulic conductivity: From petrophysical properties to aquifer geometries—A review, *Surv. Geophys.*, **28**(2–3), 169–197.
- Slater, L. & Binley, A., 2006. Synthetic and field-based electrical imaging of a zerovalent iron barrier: Implications for monitoring long-term barrier performance, *Geophysics*, **71**(5), B129–B137.
- Slater, L., Binley, A.M., Daily, W. & Johnson, R., 2000. Cross-hole electrical imaging of a controlled saline tracer injection, *J. appl. Geophys.*, **44**(2–3), 85–102.
- Tiraferrri, A., Hernandez, L.A.S., Bianco, C., Tosco, T. & Sethi, R., 2017. Colloidal behavior of goethite nanoparticles modified with humic acid and implications for aquifer reclamation, *J. Nanopart. Res.*, **19**(3), 107, doi:10.1007/s11051-017-3814-x.
- Tosco, T., Papini, M.P., Viggì, C.C. & Sethi, R., 2014. Nanoscale zerovalent iron particles for groundwater remediation: a review, *J. Cleaner Prod.*, **77**, 10–21.
- Tosco, T. & Sethi, R., 2010. Transport of non-Newtonian suspensions of highly concentrated micro-and nanoscale iron particles in porous media: a modeling approach, *Environ. Sci. Technol.*, **44**(23), 9062–9068.
- Trujillo-Reyes, J., Peralta-Videa, J.R. & Gardea-Torresdey, J.L., 2014. Supported and unsupported nanomaterials for water and soil remediation: are they a useful solution for worldwide pollution? *J. Hazard. Mater.*, **280**, 487–503.
- Ustra, A., Slater, L., Ntarlagiannis, D. & Elis, V., 2012. Spectral induced polarization (SIP) signatures of clayey soils containing toluene, *Near Surf. Geophys.*, **10**(6), 503–515.
- Vecchia, E.D., Luna, M. & Sethi, R., 2009. Transport in porous media of highly concentrated iron micro-and nanoparticles in the presence of xanthan gum, *Environ. Sci. Technol.*, **43**(23), 8942–8947.
- Velimirovic, M. *et al.*, 2014. Field assessment of guar gum stabilized microscale zerovalent iron particles for in-situ remediation of 1, 1, 1-trichloroethane, *J. Contam. Hydrol.*, **164**, 88–99.
- Ward, S.H., 1990. Resistivity and induced polarization methods, *Geotech. Environ. Geophys.*, **1**, 147–189.
- Waxman, M.H. & Smits, L.J.M., 1968. Electrical conductivities in oil-bearing shaly sands, *Society of Petroleum Engineers Journal*, **8**(2), 107–122.
- Weigand, M., Flores Orozco, A. & Kemna, A., 2017. Reconstruction quality of SIP parameters in multi-frequency complex resistivity imaging, *Near Surface Geophysics*, **15**(2), pp. 187–199.

- Weller, A., Zhang, Z. & Slater, L., 2015. High-salinity polarization of sandstones, *Geophysics*, **80**(3), D309–D318.
- Williams, K.H. *et al.*, 2009. Geophysical monitoring of coupled microbial and geochemical processes during stimulated subsurface bioremediation, *Environ. Sci. Technol.*, **43**, 6717–6723.
- Wong, J., 1979. An electrochemical model of the induced-polarization phenomenon in disseminated sulfide ores, *Geophysics*, **44**, 1245–1265.
- Xu, P. *et al.*, 2012. Use of iron oxide nanomaterials in wastewater treatment: a review, *Sci. Total Environ.*, **424**, 1–10.

5 SUPPORTING INFORMATION

Supplementary data are available at *GJI* online.

Appendix A.docx

Please note: Oxford University Press is not responsible for the content or functionality of any supporting materials supplied by the authors. Any queries (other than missing material) should be directed to the corresponding author for the paper.